Improving Rigid 3-D Calibration for Robotic Surgery

Andrea Roberti, Nicola Piccinelli, *Graduate Student Member, IEEE*, Daniele Meli, Riccardo Muradore, *Member, IEEE*, and Paolo Fiorini, *Life Fellow, IEEE*

***Abstract*—Autonomy is the next frontier of research in robotic surgery and its aim is to improve the quality of surgical procedures in the next future. One fundamental requirement for autonomy is advanced perception capability through vision sensors. In this article, we propose a novel calibration technique for a surgical scenario with a da Vinci® Research Kit (dVRK) robot. Camera and robotic arms calibration are necessary to precise position and emulate expert surgeon. The novel calibration technique is tailored for RGB-D cameras. Different tests performed on relevant use cases prove that we significantly improve precision and accuracy with respect to state of the art solutions for similar devices on a surgical-size setups. Moreover, our calibration method can be easily extended to standard surgical endoscope used in real surgical scenario.**

***Index Terms*—Surgical robotics, calibration, multi arm calibration.**

I. Introduction

A significant part of current research in Robotic-assisted Minimally Invasive Surgery (R-MIS) is focussing on the development of autonomous systems for the execution of repetitive surgical steps, such as suturing, ablation and microscopic image scanning [1]. This would potentially help surgeons, who could focus on the more cognitive demanding parts of the procedure, leaving repetitive actions to the robot. Autonomy requires systems with advanced perception, reasoning and motion planning, as highlighted in [2], [3]. Specifically, better medical imaging and vision techniques have significantly improved the performance of robotic surgical systems in a range of clinical scenarios, such as orthopaedics and neurosurgery [4]. Vision systems can retrieve pre and intra operative information from tomography (CT) [5], magnetic resonance (MR) and ultrasound to plan toll trajectories and support surgeons' decision making. However, image-guided interventions require an accurate calibration to map poses of robots, instruments and anatomy to a common reference frame. Hand-eye calibration has been widely studied within the robotics literature [6]. In R-MIS systems, where the patient-side arms are constrained by a Remote Center of Motion (RCM), it is challenging to obtain the camera motion range needed to guarantee an accurate calibration. Wang *et al.* [7] takes advantage of this constraint by finding a unique relationship between the endoscope and the surgical tool using camera perspective projection geometry. A different approach is followed in [8], [9] where the instruments themselves are used as calibration tools. Thus far, several closed-form solutions for 2d images have been proposed for hand-eye calibration that use linear methods that separate rotations and translations. In [10], the orientation component was derived by utilizing the angle-axis formulation of rotation, then the translational component was estimated using standard linear systems techniques. Chou and Kamel [11] introduced quaternions to represent orientation and solved the quaternion coefficients as a homogeneous linear least squares problem. A closed form solution was then derived using the generalized inverse method with singular value decomposition analysis. Other works [12]–[14] used the Kronecker product to get a homogeneous linear equation for the rotation matrix. However, separating the rotational and translational components neglects the intrinsic correlation between them. Working directly in 3D space is then a better solution. In [15] the authors studied the comparison between hand-eye calibration based on 2D and 3D images, introducing quantitative 2D and 3D error metrics to assess the calibration accuracy. They proved that the 3D calibration approach provides more accurate results on average but requires burdensome manual preparation and much more computation time than 2D approaches. Kim used 3D measurements at the center of markers for the hand-eye calibration [16]. Fuchs [17] proposed a solution based on depth measurements instead of 2D images, using a calibration plane with known position and orientation. The hand-eye calibration was then obtained by estimating the best fitting calibration plane of the measured depth values.

In this article, we propose a novel calibration method for the surgical robotic scenario using the da Vinci® Research Kit (dVRK) and an RGB-D camera. Differently from [17], the accuracy and computational time of our method do not depend on the placement of the calibration board within the workspace. We perform exhaustive experimental validation on relevant use cases for surgery. We separate the calibration of the robotic arms (two Patient-Side Manipulators, PSM1 and PSM2, and an Endoscope Camera Manipulator, ECM) from the hand-eye calibration of the camera. For both calibrations we propose a three-step method with closed-form solution:

1) touching reference points on a custom calibration board with the end-effectors of the surgical robot.
2) recognizing the same reference points with the RGB-D camera.
3) mapping the poses reached by the robotic arms in the first step to the 3D points computed in the second step.

The main advantage of the proposed method is the improved accuracy in a 3D metric space, which is increased by a factor of four with respect to the state-of-the-art results with comparable sensors [15]. Moreover, with our method the camera can be mounted on the moving endoscopic arm of the dVRK, overcoming the limitations of a fixed camera.

This article is organized as follows. In Section II and Section III we describe our calibration technique and the setup used to test our method. In Section IV we describe the validation of the proposed method by evaluating the workspace through simple kinematic tasks. We also compare our calibration method with Tsai's [18], which is the gold standard for hand-eye calibration, in two different tasks: grasping and camera projection to 3D space. In Section V we present our conclusions and plans for future works.

II. Proposed Method

The aim of the calibration procedure is twofold. First, we perform computation of the rigid transformations $T^{w}_{\star}$ between the common reference frame (*world*) and the base frame of the arms, $\star \in \{ecm_b, psm_{1b}, psm_{2b}\}$. Second, we estimate the transformation T^{cam}_{ecm} between the camera reference frame and the ECM reference frame. The resulting transformation tree is shown in Figure 1.

Manuscript received July 15, 2020; revised September 16, 2020 and October 14, 2020; accepted October 19, 2020. Date of publication October 26, 2020; date of current version November 20, 2020. This article was recommended for publication by Associate Editor D. Elson and Editor P. Dario upon evaluation of the reviewers' comments. This work was supported in part by the European Research Council through the European Union's Horizon 2020 Research and Innovation Programme under Grant 742671 (ARS), and in part by the European Union's Horizon 2020 Research and Innovation Programme under Grant 779813 (SARAS). *(Corresponding author: Andrea Roberti.)*

The authors are with the Department of Computer Science, University of Verona, 37135 Verona, Italy (e-mail: andrea.roberti@univr.it).

Digital Object Identifier 10.1109/TMRB.2020.3033670

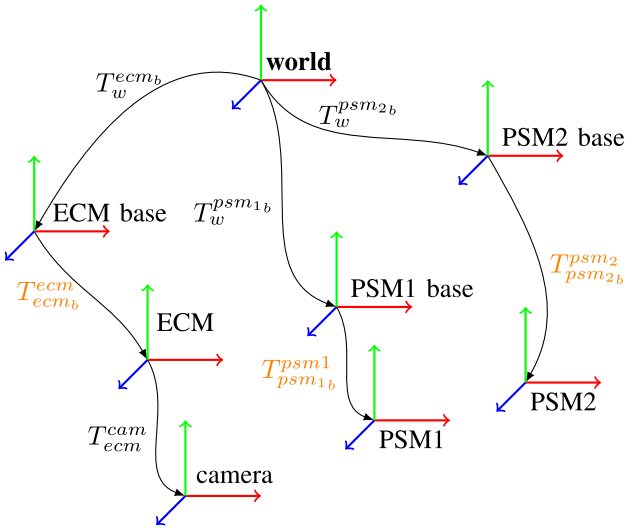

Fig. 1. The reference frames produced by our proposed method (the axes direction of the reference frames are only for visualisation purpose). The orange transformations are known, whereas the black transformations are to be estimated.

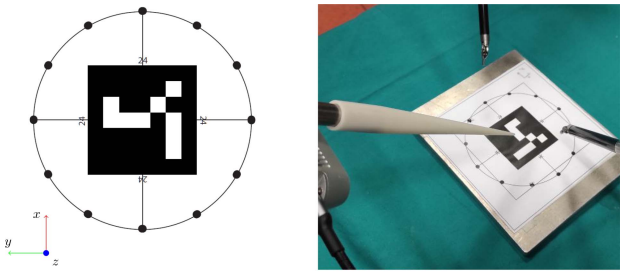

(a) Calibration pattern (b) ECM adapter

Fig. 2. The calibration components. a) the calibration board with the marker, the coloured axes represents the common reference frame directions b) the adapter for the ECM positioning.

We use a custom calibration board, shown in Figure 2(a), with an ArUco marker in the center of a circumference of 50 mm radius, with several reference dots. We equipped the ECM with a 3D-printed adapter, shown in Figure 2(b). The adapter has a smaller tip than the ECM to guarantee precise positioning on the dots on the board.

The procedure starts by positioning the calibration board in the robot workspace. We choose a set of reference points P such that each point $p \in P$ is reachable by the three arms and visible from the camera. The points in P must be symmetric with respect to the center of the board to compute the origin of the common reference frame; at least three points are needed to estimate the plane coefficients. The best fitting plane is characterized by the centroid of the point set P, $\mathbf{c}$, and the normal vector $\mathbf{n}$. Their optimal estimations are the solution of the optimisation problem

$$\{\hat{\mathbf{c}}, \hat{\mathbf{n}}\} = \underset{\mathbf{c}, |\mathbf{n}|_2=1}{\arg\min} \sum_{i=1}^{n} \Big((\mathbf{p}_i - \mathbf{c})^T \mathbf{n} \Big)^2 \tag{1}$$

As in [19] the centroid is estimated by

$$\hat{\mathbf{c}} = \frac{1}{n} \sum_{i=1}^{n} \mathbf{p}_i. \tag{2}$$

The normal vector $\mathbf{n}$ is obtained by factorizing the distance matrix A with Singular Value Decomposition (SVD)

$$A = USV^T = \big[\mathbf{p}_1 - \hat{\mathbf{c}}, \dots \mathbf{p}_n - \hat{\mathbf{c}}\big] \in \mathbb{R}^{3\times n} \tag{3}$$

and taking the third column of the matrix $U = \begin{bmatrix}\mathbf{u}_1 & \mathbf{u}_2 & \mathbf{u}_3\end{bmatrix}$, $\hat{\mathbf{n}} = \mathbf{u}_3$. To generate a common reference frame for all the tools we implement the following three main steps:

(1) Arm calibration
(2) Camera calibration
(3) Hand-eye calibration.

A. Arm Calibration

To find the transformation of the arms base frame with respect to the common reference frame we record the end effector pose of the arms (PSMs and ECM with adapter) on each point in the set P. In order to obtain the ECM effective pose, we remove the known rigid transformation between the adapter and the ECM. On this set we estimate the best fitting plane using (1). The set P is then augmented by adding a point above the calibration board acquired by moving the arm's end effector. This last point is used to define the desired plane normal direction

$$\mathbf{n}_d = \frac{\mathbf{p}_{n+1} - \mathbf{c}}{|\mathbf{p}_{n+1} - \mathbf{c}|_2}$$

where $\mathbf{p_{n+1}}$ is the last point in the ordered set P, $\mathbf{c}$ is the centroid of P and $|*|_2$ is the vector norm. For each arm, the homogeneous transformation $T_\star^w$ of the common reference with respect to the arm base frame is defined using the direction versors

$$\begin{aligned}\mathbf{u} &= \text{sign}(\mathbf{n} \cdot \mathbf{n_d})\mathbf{n} \\ \mathbf{l} &= \mathbf{u} \times \frac{\mathbf{p}_1 - \mathbf{c}}{|\mathbf{p}_1 - \mathbf{c}|_2} \\ \mathbf{f} &= \mathbf{l} \times \mathbf{u}\end{aligned}$$

and the centroid $\mathbf{c}$,

$$T_\star^w = \begin{bmatrix} \mathbf{f}_x & \mathbf{l}_x & \mathbf{u}_x & \mathbf{c}_x \\ \mathbf{f}_y & \mathbf{l}_y & \mathbf{u}_y & \mathbf{c}_y \\ \mathbf{f}_z & \mathbf{l}_z & \mathbf{u}_z & \mathbf{c}_z \\ 0 & 0 & 0 & 1 \end{bmatrix}.$$

B. Camera Calibration

To find the transformation T_{cam}^w for the RGB-D camera we first detect the center of the ArUco marker on the board with respect to the camera frame. Once we find a camera position that ensures good visibility and a stable pose of the ArUco marker, we align the pose on the point cloud generated from the depth map acquired by the RGB-D camera. We use the marker pose and its known radius to generate the pose of every dot in the set P in the marker reference frame, as well as the point above the calibration board.

Once the pose set P is obtained we find the best fitting plane using (1) and then we build the homogeneous transformation T_{cam}^w between the common reference frame to the camera base frame by adapting the previous approach used for the arms.

C. Hand-Eye Calibration

The hand-eye calibration problem is formulated using the homogeneous transformation matrices:

$$AX = XB$$

where A and B are known homogeneous matrices representing the frames of the base of the robot and the camera, respectively. The unknown transformation X is between the robot coordinate frame and the camera coordinate frame. Given T_{cam}^w, we can compute X as the relative homogeneous transformation between the end effector of the ECM and the RGB-D base frame:

$$T_{ecm}^{cam} = T_w^{cam} \big(T_w^{ecm}\big)^{-1}.$$

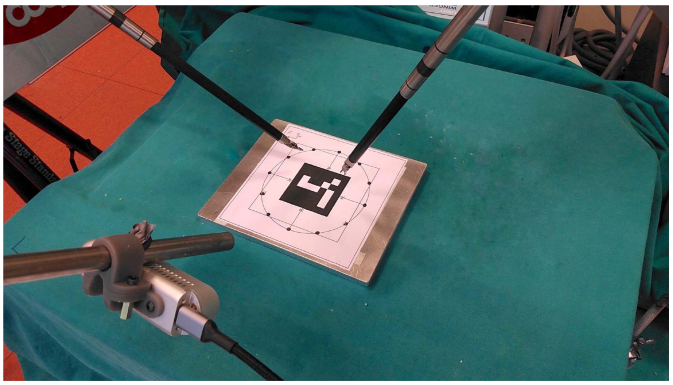

Fig. 3. The proposed setup for calibration, with the RealSense d435, the PSMs and the calibration pattern.

TABLE I
REALSENSE D435 SPECIFICATIONS

Camera specifications	
Resolution	1280×720
Field of view (FOV)	$91° \times 65° \times 100°$
Frame rate	90 fps
Baseline	50 mm
Z-accuracy	$\leq 2\%$ of the working distance

III. EXPERIMENTAL SETUP

The validation of the proposed method has been carried out with the dVRK robot shown in Figure 3.

The stereo endoscope has been augmented with an Intel RealSense d435 RGB-D camera rigidly attached to the endoscope through a 3D printed adapter. The camera specifications are reported in Table I. The whole calibration method has been implemented in Robot Operating System (ROS) using the Point Cloud Library (PCL) and OpenCV. The present setup is not compatible with a surgical scenario. However it is well possible that in the near future small RGBD cameras could be integrated within the endoscope.

IV. EXPERIMENTAL RESULTS

To experimentally validate our methodology we compared our calibration with the Tsai's method [18] in two benchmark tests for surgical robotics:

- Localization and grasping of small targets,
- Dual-arm manipulation

Finally we evaluated the accuracy of the projection from 2D camera image plane to the 3D workspace.

A. Localization and Grasping

In the first scenario (Figure 4) the two PSMs must autonomously grasp a ring placed on the calibration board, in this case on location 2. The RGB-D camera identifies the point cloud corresponding to the ring after color and shape segmentation, and points are transformed from the camera to the common reference frame. The ring has a diameter of 15 mm, and the target point for both PSMs is chosen as the center of the ring. The ring is placed in the 9 different locations on the board to cover the full $x-y$ plane, as shown in Figure 4. The arms reach the target points ten times, and for each iteration we compute the Euclidean distance between the target and the final positions of the PSMs. In this way, we estimate the mean accuracy of our calibration procedure on the $x-y$ plane. The results are reported in Figure 5 and compared with state-of-the-art Tsai's calibration method [18]. It is worth mentioning that errors are comprehensive of the estimated kinematic accuracy of the da Vinci® : 1.02 mm on average when localizing and reaching fiducial markers [20], with a maximum error of 2.72 mm [21].

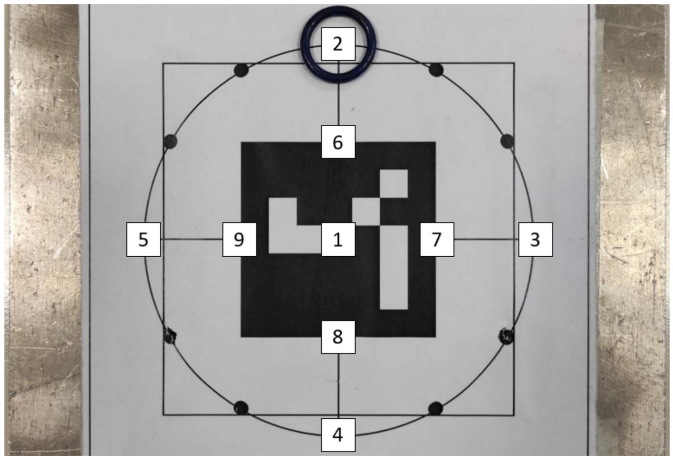

Fig. 4. Setup for the localization and grasping experiment. The numbers on calibration board represents the nine locations used during the experiment. The ring is identified by the camera and then reached by the PSMs.

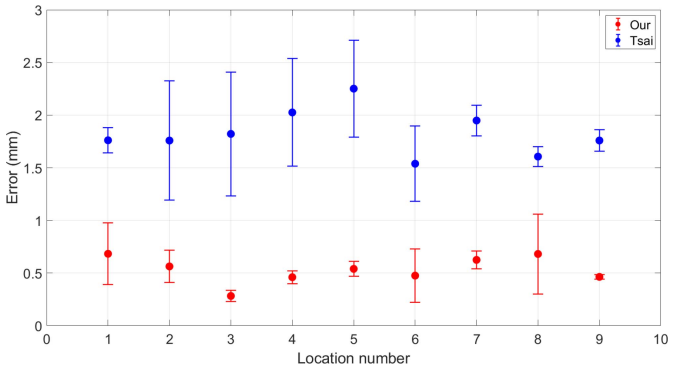

Fig. 5. The measured 3D positioning errors between the robot end effector and the grasping point.

TABLE II
A COMPARISON OF THE ERROR IN THE LOCALIZATION AND GRASPING TEST

	Max error (mm)	Mean error (mm)	Std dev (mm)
Our method	1.07	0.53	0.15
Tsai [18]	3.17	1.83	0.33

Table II shows that our method achieves significantly better accuracy (0.53 mm average error against 1.83 mm with Tsai's calibration). The error does not depend on the location of the ring on the $x-y$ plane.

B. Dual Arm Manipulation

In the second scenario (Figure 6) the PSMs start holding the same ring, and they must execute simultaneous pre-computed circular trajectories with center on the z axis of the common reference frame (45 mm above the calibration board) and radius r ranging from 10 mm to 40 mm. Circumferences are first defined in the $x-z$ plane of the common reference frame (normal to the calibration board), and then replicated in planes rotated around the z axis with a step of 10 deg. In this way we define a spherical workspace by interpolation between the recorded trajectories. PSMs are commanded with the transformed waypoints in their relative frames. This task validates the accuracy of the transformations between the arms computed with the proposed method. We measure the difference between the trajectories

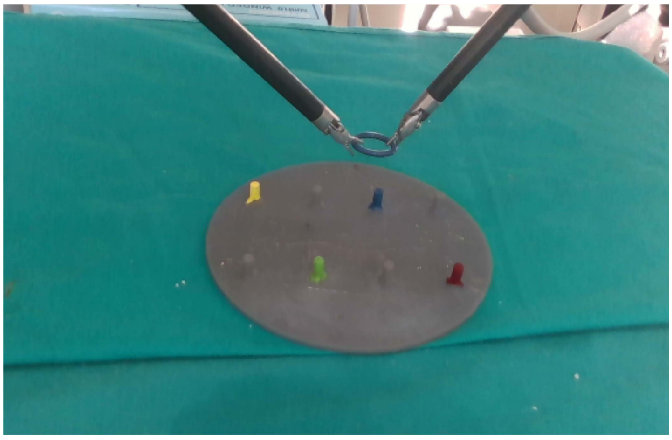

Fig. 6. Dual arm manipulation experiment. The two arms carries a ring while performing circular trajectories through the workspace.

of the two PSMs, and we consider the standard and the maximum deviations from the mean for each radius. In absence of calibration and kinematic errors, the difference between the trajectories would have null standard deviation. Figure 7 shows the absolute error through the workspace for spheres with radii 20 mm, 30 mm and 40 mm, by using the Lambert equal-area cylindrical projection [22]. In Table III we report the errors for all the spheres. We notice that the mean error increases with the radius of the sphere, as the PSMs move away from the calibration plane. The standard deviation of the error increases with the radius but remains below 0.11 mm, hence the overall error does not change significantly on the surface of the spheres. This ensures good repeatability of motions in the whole workspace. The accuracy of our calibration method in 3D is compatible with the requirements of surgery (the mean error between the arms is below 1 mm, comparable with the known kinematic accuracy of the da Vinci®).

C. 2D/3D Projection

In the last scenario the PSM1, with a colored marker on its tip, executes a spiral-shaped trajectory along the entire workspace. The RGB-D camera identifies the marker in the image plane, and the corresponding 3D point can be computed using the depth value. The trajectory starts near the origin of the common reference frame and then increases in radius and altitude according to the following parametric equations

$$\begin{aligned} x(t) &= \kappa t \cos(\omega t) \\ y(t) &= \kappa t \sin(\omega t) \\ z(t) &= \kappa t \end{aligned}$$

where ω is the constant angular speed and $\kappa \in \mathbb{R}$ is a time-scaling factor. The orientation of the end effector is kept fixed towards the camera along the trajectory. We measure the Euclidean error between the points in the trajectory executed by the arm and the re-projected points from the camera image plane. Figure 8 and Table IV show that the re-projection accuracy with our method significantly outperforms the one reached with Tsai's. In fact, the mean error (4.71 mm) and the maximum error (11.76 mm) are four and two times smaller than the one achieved by Tsai's method. It is important to remark that the measured error also includes the marker detection accuracy.

Finally Figure 9 shows the re-projection of PSMs end effector position onto the camera image plane with both calibration methods. Our method achieves a better re-projection better of the 3D instruments.

V. Conclusion

In this article we proposed a novel 3D calibration procedure for the patient-side manipulators and the ECM of the da Vinci® surgical robot. Our procedure exploits an RGB-D Realsense camera. We have validated our calibration procedure by evaluating the 2D/3D projection errors on two relevant use cases for surgery localization and grasping of a small object and dual-arm manipulation. Both tasks require an accurate estimation of the transformation tree connecting the arms and the camera, to guarantee precise positioning

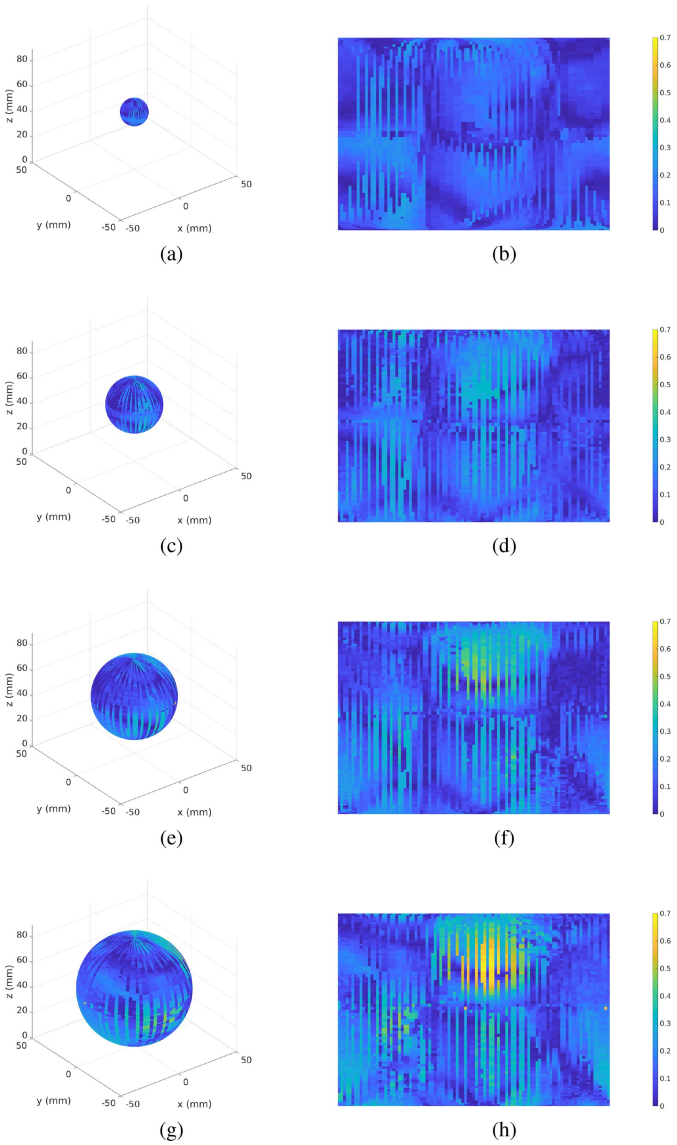

Fig. 7. Absolute error of the dual arm manipulation through the workspace. The workspace has been projected using the Lambert equal-area cylindrical projection, the error is reported in mm. a) the workspace surface of the sphere with radius 10 mm, b) the projected surface of the sphere with radius 10 mm, c) the workspace surface of the sphere with radius 20 mm, d) the projected surface of the sphere with radius 20 mm, e) the workspace surface of the sphere with radius 30 mm, f) the projected surface of the sphere with radius 30 mm, g) the workspace surface of the sphere with radius 40 mm, h) the projected surface of the sphere with radius 40 mm.

TABLE III
THE POSITIONING ERROR BETWEEN THE PSM1 AND PSM2 DURING THE DUAL-ARM MANIPULATION EXPERIMENT

Radius (mm)	Max error (mm)	Mean error (mm)	Std dev (mm)
10	0.61	0.11	0.06
20	0.37	0.13	0.08
30	0.51	0.14	0.10
40	0.62	0.16	0.11

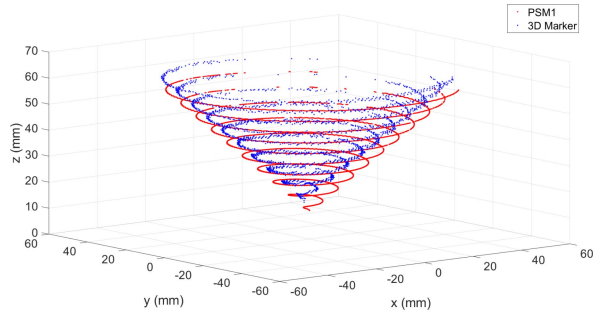

(a)

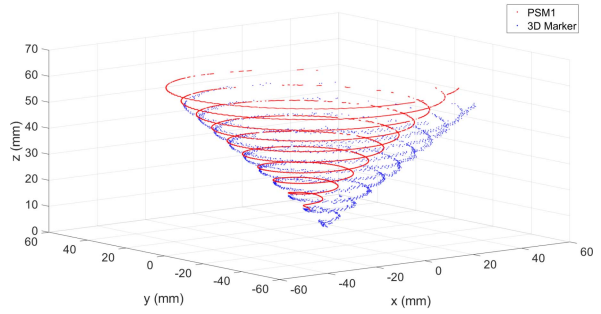

(b)

Fig. 8. Spiral-shaped trajectory executed by the PSM1 with our method in (a) and Tsai's method in (b). The red trajectory represents the kinematics of the PSM1, while the blue trajectory represents the marker identified in 3D space.

TABLE IV
A COMPARISON OF THE ERROR BETWEEN THE MARKER TIP TRAJECTORY AND THE MEASURED TIP TRAJECTORY FOR THE PROJECTION TEST

	Max error (mm)	Mean error (mm)	Std dev (mm)
Our method	11.76	4.71	0.89
Tsai [18]	20.85	16.41	1.21

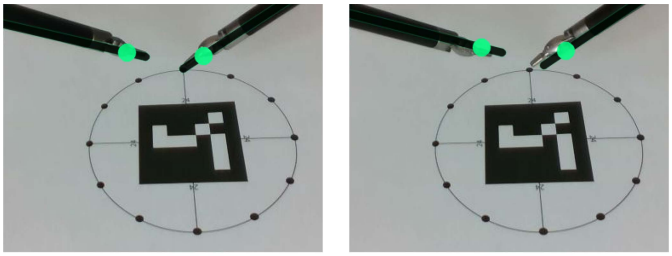

(a) Our method (b) Tsai's method

Fig. 9. An example of re-projection of da Vinci® surgical instruments by using kinematic re-projection of the model directly onto camera color image.

and coordination of the PSMs. In our experiments the proposed method outperforms the state-of-the-art solution proposed by Tsai. Our method reaches an accuracy below 1 mm on the $x-y$ plane and in the dual arm manipulation scenario, which is comparable with the intrinsic kinematic precision of the da Vinci®.

The main drawback of our solution is the use of a RGB-D camera, which limits its actual application in surgery. We think that our methodology can be extended to a setup with a standard surgical endoscope. The main issue with an endoscope is that the small baseline between the stereo cameras introduces additional complexities in computing depth maps and reduces the depth range of view. We will address this problem in our future research. Moreover, we will develop an autonomous procedure for our calibration method, which can significantly reduce manual errors and simplify its implementation in a surgical setup.

REFERENCES

[1] X. Du *et al.*, "Combined 2D and 3D tracking of surgical instruments for minimally invasive and robotic-assisted surgery," *Int. J. Comput. Assist. Radiol. Surg.*, vol. 11, no. 6, pp. 1109–1119, 2016.

[2] P. Fiorini *et al.*, "Challenges of autonomous robotic surgery," in *Proc. Hamlyn Symp. Med. Robot. (HSMR)*, 2019.

[3] G. De Rossi *et al.*, "Cognitive robotic architecture for semi-autonomous execution of manipulation tasks in a surgical environment," in *Proc. IEEE/RSJ Int. Conf. Intell. Robots Syst. (IROS)*, Macau, China, 2019, pp. 7827–7833.

[4] T. K. Adebar, A. E. Fletcher, and A. M. Okamura, "3-D ultrasound-guided robotic needle steering in biological tissue," *IEEE Trans. Biomed. Eng.*, vol. 61, no. 12, pp. 2899–2910, Dec. 2014.

[5] N. Piccinelli *et al.*, "Rigid 3D registration of pre-operative information for semi-autonomous surgery," in *Proc. Int. Symp. Med. Robot.*, Atlanta, USA, 2020.

[6] M. Shah, R. D. Eastman, and T. Hong, "An overview of robot-sensor calibration methods for evaluation of perception systems," in *Proc. Workshop Perform. Metrics Intell. Syst.*, 2012, pp. 15–20.

[7] Z. Wang *et al.*, "Vision-based calibration of dual RCM-based robot arms in human-robot collaborative minimally invasive surgery," *IEEE Robot. Autom. Lett.*, vol. 3, no. 2, pp. 672–679, Apr. 2018.

[8] K. Pachtrachai, M. Allan, V. Pawar, S. Hailes, and D. Stoyanov, "Hand-eye calibration for robotic assisted minimally invasive surgery without a calibration object," in *Proc. IEEE/RSJ Int. Conf. Intell. Robots Syst. (IROS)*, Daejeon, South Korea, 2016, pp. 2485–2491.

[9] F. Zhong, Z. Wang, W. Chen, K. He, Y. Wang, and Y.-H. Liu, "Hand-eye calibration of surgical instrument for robotic surgery using interactive manipulation," *IEEE Robot. Autom. Lett.*, vol. 5, no. 2, pp. 1540–1547, Apr. 2020.

[10] Y. C. Shiu and S. Ahmad, "Calibration of wrist-mounted robotic sensors by solving homogeneous transform equations of the form AX=XB," *IEEE Trans. Robot. Autom.*, vol. 5, no. 1, pp. 16–29, Feb. 1989.

[11] J. C. Chou and M. Kamel, "Finding the position and orientation of a sensor on a robot manipulator using quaternions," *Int. J. Robot. Res.*, vol. 10, no. 3, pp. 240–254, 1991.

[12] R.-H. Liang and J.-F. Mao, "Hand-eye calibration with a new linear decomposition algorithm," *J. Zhejiang Univ. Sci. A*, vol. 9, no. 10, pp. 1363–1368, 2008.

[13] H. Pan, N. L. Wang, and Y. S. Qin, "A closed-form solution to eye-to-hand calibration towards visual grasping," *Ind. Robot Int. J.*, vol. 41, no. 6, pp. 567–574, 2014.

[14] M. Najafi, N. Afsham, P. Abolmaesumi, and R. Rohling, "A closed-form differential formulation for ultrasound spatial calibration: Multi-wedge phantom," *Ultrasound Med. Biol.*, vol. 40, no. 9, pp. 2231–2243, 2014.

[15] S. Kahn, D. Haumann, and V. Willert, "Hand-eye calibration with a depth camera: 2D or 3D?" in *Proc. IEEE Int. Conf. Comput. Vis. Theory Appl. (VISAPP)*, vol. 3. Lisbon, Portugal, 2014, pp. 481–489.

[16] D. W. Kim and J. E. Ha, "Hand/eye calibration using 3D–3D correspondences," in *Applied Mechanics and Materials*, vol. 319. Dürnten, Switzerland: Trans. Tech. Publ., 2013, pp. 532–535.

[17] S. Fuchs, "Calibration and multipath mitigation for increased accuracy of time-of-flight camera measurements in robotic applications," Ph.D. dissertation, Dept. Fakultät für Elektrotechnik und Informatik, Universitätsbibliothek der Technischen Universität Berlin, Germany, 2012.

[18] R. Y. Tsai and R. K. Lenz, "A new technique for fully autonomous and efficient 3D robotics hand/eye calibration," *IEEE Trans. Robot. Autom.*, vol. 5, no. 3, pp. 345–358, Jun. 1989.

[19] W. Gander and J. Hrebicek, *Solving Problems in Scientific Computing Using Maple and MATLAB®*. Heidelberg, Germany: Springer, 2011.

[20] T. Haidegger, P. Kazanzides, I. Rudas, B. Benyó, and Z. Benyó, "The importance of accuracy measurement standards for computer-integrated interventional systems," in *Proc. EURON GEM Sig Workshop Role Exp. Robot. Res. IEEE ICRA*, 2010, pp. 1–6.

[21] D. M. Kwartowitz, S. D. Herrell, and R. L. Galloway, "Toward image-guided robotic surgery: Determining intrinsic accuracy of the da Vinci robot," *Int. J. Comput. Assist. Radiol. Surg.*, vol. 1, no. 3, pp. 157–165, 2006.

[22] M. O. Ward, G. Grinstein, and D. Keim, *Interactive Data Visualization: Foundations, Techniques, and Applications, Second Edition—360 Degree Business*, 2nd ed., A. K. Peters, Ltd., 2015.